



HAL
open science

Imaging of alumina supports by laser-induced breakdown spectroscopy: A new tool to understand the diffusion of trace metal impurities

Florian Trichard, Florine Gaulier, Jérémie Barbier, Didier Espinat, Bertrand Guichard, Charles-Philippe Lienemann, Loic Sorbier, Pierre Levitz, Vincent Motto-Ros

► To cite this version:

Florian Trichard, Florine Gaulier, Jérémie Barbier, Didier Espinat, Bertrand Guichard, et al.. Imaging of alumina supports by laser-induced breakdown spectroscopy: A new tool to understand the diffusion of trace metal impurities. *Chinese Journal of Catalysis*, 2018, 363, pp.183-190. 10.1016/j.jcat.2018.04.013 . hal-01978484

HAL Id: hal-01978484

<https://ifp.hal.science/hal-01978484>

Submitted on 11 Jan 2019

HAL is a multi-disciplinary open access archive for the deposit and dissemination of scientific research documents, whether they are published or not. The documents may come from teaching and research institutions in France or abroad, or from public or private research centers.

L'archive ouverte pluridisciplinaire **HAL**, est destinée au dépôt et à la diffusion de documents scientifiques de niveau recherche, publiés ou non, émanant des établissements d'enseignement et de recherche français ou étrangers, des laboratoires publics ou privés.

Imaging of alumina supports by laser-induced breakdown spectroscopy: A new tool to understand the diffusion of trace metal impurities

Florian Trichard[#], Florine Gaulier[§], Jeremie Barbier[§], Didier Espinat[§], Bertrand Guichard[§], Charles-Philippe Lienemann[§], Loïc Sorbier^{§*}, Pierre Levitz^l, Vincent Motto-Ros[§]

[#]Ablatom, Bâtiment Kastler, Domaine Scientifique de la DOUA, 10 Rue Ada Byron, 69 622 Villeurbanne Cedex, France

[§]IFP Energies nouvelles, Rond-Point de l'échangeur de Solaize, BP 3, 69360 Solaize, France

^lLaboratoire PHENIX UMR 8234, Université Pierre et Marie Curie, Case Courrier 51, 4 place Jussieu 75252 Paris Cedex 5, France

[§]Institut Lumière Matière UMR 5306, Université Lyon 1 - CNRS, Université de Lyon 69622 Villeurbanne, France

Keywords:

LIBS, Trace elements, imaging, asphaltenes

Abstract

Imaging the distribution of reactive molecules in an internal diffusion-limited catalyst is of primary importance in the comprehension and modeling of these systems. Mesoporous alumina supports were impregnated with asphaltenes in a self-pressurized autoclave at high pressure (5 MPa) and high temperature (523 K). Extrudates were then analyzed by laser-induced breakdown spectroscopy (LIBS). We showed that LIBS can provide quantitative concentration maps of sulfur, nickel and vanadium in the ppm range. Processing of these maps is proposed to obtain one-dimensional profiles of the penetration of these elements. These profiles show that the penetration of asphaltenes into the catalyst support is a very complex process. These findings contribute to improving the comprehension of internal diffusion-limited processes, particularly the hydrodemetallization (HDM) process of oil residues. This report also indicates that LIBS-based

imaging represents a powerful tool for quickly providing two-dimensional elemental maps over a large dynamic range, i.e., typically from ppm to tens of %, thereby opening up opportunities for innumerable applications in the field of catalysis.

1 Introduction

Heterogeneous catalysis plays an essential role in the industrial synthesis of chemicals. More than 80% of all chemicals have been processed through at least one heterogeneous catalytic process.¹ Since the development of spatially resolved techniques, imaging the spatial heterogeneities of catalysts has been a long-standing goal.² In particular, characterization of the local elemental composition of catalysts provides insight essential for their rational design. For heterogeneous catalytic process under internal diffusion limitations, the imaging of the adsorbed reactants at the grain scale would be of primary importance for the understanding and modeling of such processes. Among the industrially relevant processes under severe internal diffusion limitations, the hydrodemetallization (HDM) of oil residues is one of the most striking and well documented.³ The HDM of oil residues is performed in fixed or ebullated beds using alumina-supported catalysts.⁴ Metal precursors (mostly nickel and vanadium) are known to originate mainly from asphaltenes, polyaromatic macromolecules that may self-assemble.⁵ The internal diffusion limitation of metal deposits is assessed by the egg-shell profiles of nickel and vanadium on aged catalysts.⁶⁻⁸

Imaging the distribution of asphaltenes in catalysts before the reaction step should allow the establishment of models for their transport at the grain scale. However, no quantitative elemental distribution of Ni and V species has yet been reported. Only indirect measurements are available in the literature, and these indirect measurements are sensitive to the validity of the model employed to interpret them. For example, the transport of asphaltenes in HDM catalysts can be studied by supernatant concentration measurements in a batch cell at ambient temperature.⁹⁻¹² The use of a self-pressured autoclave allowed the uptake kinetics to be obtained under near process-relevant conditions (523 K, 5 MPa).¹³ Concentration profiles in the catalyst pellets may be acquired through the modeling of the transport at the pellet scale. Optical microscopy of the cross-section of pellets provides qualitative information on the penetration profile of asphaltenes in the grain.¹⁰ However, because the dark coloration is only qualitative, it is not easily convertible to the local concentration of asphaltenes and is impossible to correlate with the local concentration of metals. As the metal contents in asphaltenes are in the hundreds of ppm range and the adsorption

of asphaltenes on catalysts at saturation is on the order of a few mass percent, a metal concentration of a few ppm is expected on the adsorbed supports. Despite large efforts to develop spatially resolved analytical techniques, few analytical techniques can combine high spatial resolution and low detection limits to image these trace metals. Among the standard techniques used, electron probe microanalysis suffers from a low intrinsic sensitivity and its operation under secondary vacuum conditions where adsorbed species may desorb.¹⁴ X-ray microfluorescence operated with a synchrotron source is limited by the availability of reference samples and the accessibility of beam runs.¹⁵

In this paper, we proposed evaluating a novel imaging technology based on laser-induced breakdown spectroscopy (LIBS). This method has the advantages of fast imaging, high sensitivity and relevant spatial resolution to characterize the metal deposits on asphaltene-adsorbed catalyst supports. LIBS-based imaging has been already employed in biology¹⁶⁻¹⁷, geology¹⁸⁻¹⁹, post-combustion catalysis²⁰⁻²³, steel manufacturing²⁴ and surface science²⁵⁻²⁶ to image minor to trace elements. In addition, its compatibility with optical microscopy, fast operating speed, operability under ambient conditions, high dynamic range, and multi-elemental capability make this technology highly attractive for routine use. One drawback of the technique is the difficulty in obtaining calibration curves to convert detected intensities to local concentrations. Nevertheless, by careful choice of optical transitions and adequate calibration strategies, quantitative LIBS maps with a high dynamic range can be obtained.²⁷

The aim of this paper is to achieve the quantitative LIBS-based imaging of nickel, vanadium, carbon and sulfur distributions on catalyst supports impregnated with asphaltenes. The first section describes the experimental protocol to obtain catalyst supports at different impregnation times, to perform the LIBS mapping, and to carry out data processing to obtain elemental maps. The following section includes a discussion of the results, providing insight into the transport mechanism of the metal and sulfur precursors. To the best of our knowledge, this is the first time that adsorbed precursors are imaged. Not only in the particular field of petrochemistry but also in numerous other fields, this work can revolutionize our understanding of transport mechanisms at the grain scale, a necessary step to progress towards more effective catalysts under internal diffusion limitations.

2 Materials and Methods

2.1 Uptake of asphaltenes on alumina supports

Asphaltenes were extracted by *n*-heptane (Aldrich 99.5%) precipitation from a Safaniya vacuum residue according to the NF T60-115 method. The asphaltene properties are summarized in Table 1. The asphaltenes were diluted in toluene (Aldrich 99%) to produce a 2.0 wt. % solution.

Table 1: Properties of Safaniya asphaltenes

| | |
|------------------------------|-----------------|
| H/C ratio | 1.10 ± 0.05 |
| Density (g/cm ³) | 1.22 ± 0.06 |
| C content (wt %) | 82.3 ± 0.4 |
| S content (wt %) | 8 ± 2 |
| V content (ppm) | 550 ± 50 |
| Ni content (ppm) | 190 ± 30 |

Mesoporous γ -Al₂O₃ cylindrical extrudates of a 3 mm diameter and a 10 mm average length were characterized by nitrogen adsorption and mercury intrusion according to the ASTM D3663-03 and ASTM D4284-03 methods, respectively. The nitrogen adsorption was measured on a Micromeritics ASAP 2420. The specific surface area S_{BET} (in m²/g) was obtained with the Brunauer–Emmett–Teller (BET) method.²⁸ To prevent water adsorption on the samples, already dried extrudates were pretreated at 623 K for 3 h under vacuum (10⁻⁴ Pa) before measurement. The pore size distribution, which was in the 4–80 nm range, was obtained from the desorption branch of the nitrogen isotherm using the Barrett–Joyner–Halenda (BJH) method.²⁹

Table 2: Properties of the alumina support

| | |
|---|-----------------|
| Specific surface area, S_{BET} (m ² /g) | 200 ± 20 |
| Porous volume, V_{BJH} (cm ³ /g) | 0.80 ± 0.04 |
| Mean pore diameter, d_{m} (nm) | 13.7 ± 0.7 |
| Structural density, ρ_{S} (g/cm ³) | 3.01 ± 0.35 |
| Porosity, ε (%) | 69 ± 3 |

The mean pore diameter was defined as the mode of the volume-averaged pore size distribution. The structural density ρ_S is obtained from the total porous volume V_{BJH} . Mercury intrusion was performed on a Micromeritics AutoPore IV 9500 after thermal treatment (523 K for 2 h). The grain density ρ_g was obtained at a 0.2 MPa intrusion pressure, under which mercury fills only intergrain porosity, not intragrain porosity. The porosity ε (void volume fraction) was obtained from $\varepsilon = 1 - \rho_g/\rho_S$. The properties of the alumina support are summarized in Table 2.

Before measurement of the asphaltene adsorption, alumina extrudates were dried for at least 2 h at 423 K. The extrudates were weighed and placed in a self-pressurized autoclave with a controlled amount of asphaltene solution to reach the targeted pressure (5 MPa) at the chosen temperature (523 K). Details on the autoclave and the protocol have been published elsewhere.¹³ Seven experiments were performed with impregnation times varied from zero to 6 weeks. The time zero means that only the temperature increase and decrease were conducted without residence time at the targeted temperature. The temperature rise to 95% of the targeted temperature (511 K) lasted 27 min, and the return to ambient temperature lasted 16 min. After each experiment, the extrudates were separated from the supernatant by filtration through 0.45 μm filter paper. Wet supports were washed with cold toluene and dried at 423 K for 6 h. Extrudates were weighted in order to measure the mass of the impregnated asphaltenes. The concentrations of asphaltenes in the supernatant and toluene used for washing were also determined by weighting the residue after complete evaporation of toluene. Assuming that there is no segregation, the global vanadium, nickel, sulfur and carbon concentrations in pellets can be calculated by multiplying the asphaltene concentration by the element concentration in the asphaltenes.

2.2 LIBS mapping

Sample preparation was similar to the preparation typically used for optical microscopy. Impregnated extrudates were cut at their half-length and embedded in a thermoplastic acrylic resin (Buehler TransOptic) in a press (Struers ProntoPress) at 453 K and 15 kN together with a fresh extrudate used as a blank. The obtained 2.5 cm diameter resin plots were polished with SiC abrasive paper up to 4000 mesh.

The LIBS instrument used in this study has already been described in detail in a previous article.³⁰ A schematic illustration of the apparatus and of the elemental image extraction workflow is provided in Figure 1. A nanosecond Nd:YAG laser source operating at a 10 Hz repetition rate and

emitting at the fundamental wavelength (1064 nm) was employed,. The laser beam was focused vertically on the sample surface with a 15× magnification objective. In all LIBS experiments, the laser energy was set at 1 mJ. With this configuration, the typical crater size observed was less than 10 μm, which represents the ultimate attainable resolution. The resin plot was mounted on a motorized xyz stage, and the surface sample was scanned point by point. A 30 μm step size was used by adjusting the motor speed according to the 10 Hz fixed laser repetition rate. At each site, a laser pulse resulted in the vaporization of a small fraction of the material (~ 0.1 ng) and the formation of a plasma. Control and regulation of parameters such as laser energy and focusing allowed standardization of the experimental parameters throughout the LIBS experiments. Homemade software developed in the LabVIEW environment controlled the entire system and allowed the use of automated sequences to scan the region of interest.

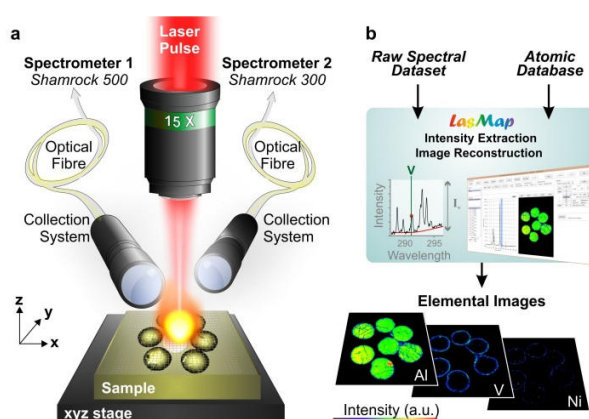


Figure 1. a Principle of LIBS-based spectral mapping. b Principle of elemental map extraction.

Two types of analysis were performed on the catalyst samples. The first analysis was focused on the elements Ni, V and C. In this case, the plasma radiation was collected by two lens-fiber systems positioned with an angle of 35° relative to the sample surface. The outputs of the fibers were connected to two independent spectrometers: a Shamrock 500 (Andor Technology) and a Shamrock 303 (Andor Technology). Each of these spectrometers was equipped with intensified CCD cameras (iStar, ICCD, Andor Technology). Spectral acquisition was performed by the synchronization between the Q-switch of the laser and the ICCD cameras.

The second analysis was focused on sulfur detection, which requires specific instrumentation since the most sensitive emission lines of sulfur are in the vacuum UV (VUV) spectral range (i.e., at 180.73 nm). In this spectral range, because oxygen in the ambient air absorbs emissions below 190 nm, the complete collection system (i.e., the path from the plasma to the spectrometer) needs to be purged with argon or helium. A homemade probe designed for VUV detection was used.²⁹ In this case, the plasma radiation was collected directly through the VUV probe and analyzed with a compact spectrometer (Maya2000Pro, Ocean Optics). The end of the probe was positioned approximately 200 μm from the plasma with an angle of 25° relative to the sample surface. The Maya2000Pro spectrometer covered a spectral range from 150 to 255 nm with a spectral resolution of 100 pm (see supplementary table 1). This spectrometer was equipped with a CCD camera (S10420, Hamamatsu) that does not allow gated detection to be performed.

All the experiments were carried out in ambient atmosphere with an argon gas flow in the plasma region (~ 1 ml/min). This allowed us both to improve the signal-to-noise ratio due to better plasma confinement²³ and to prevent any surface contamination from the deposition of ablated material from previous laser shots. The selected emission lines of each element of interest are summarized in supplementary table 2. Each sample was scanned in approximately 2 h. The seven samples (each containing 6 to 7 sections of the catalysts) were analyzed to detect Ni, V and C. Three samples were re-analyzed in the VUV configuration after slight surface polishing to detect sulfur.

2.3 LIBS data processing

Let $S(\lambda, \mathbf{x})$ be the intensity recorded at wavelength λ and position \mathbf{x} . The intensity of an emission line $I(\lambda_i, \mathbf{x})$ is obtained from the spectrum $S(\lambda, \mathbf{x})$ by subtracting the emission background $B(\lambda_i, \mathbf{x})$ computed by linear interpolation of intensities far away from the line from the intensity $S(\lambda_i, \mathbf{x})$ at the line wavelength λ_i :

$$I(\lambda_i, \mathbf{x}) = S(\lambda_i, \mathbf{x}) - B(\lambda_i, \mathbf{x})$$

A mask M of the pellet was defined for each catalyst section of each sample from its corresponding elemental image of aluminum. Aluminum is present only in the catalyst; thus, the conversion of its elemental image to a binary image provides a representative mask of the catalyst sections (see supplementary Figure 1).

As the support pellets are long extrudates, the intensity map obtained from the cross-section of their half-length is representative of the whole volume. The total spectrum of an element in the pellet is obtained from the summed spectrum on the mask:

$$S_{\Sigma}(\lambda) = \sum_{\mathbf{x} \in M} S(\lambda, \mathbf{x})$$

The total intensity $I_{\Sigma}(\lambda_i)$ of a line may be extracted from $S_{\Sigma}(\lambda_i)$ by removing the associated background. The mean total intensity $\bar{I}_{\Sigma}(\lambda_i)$ is computed from:

$$\bar{I}_{\Sigma}(\lambda_i) = \frac{I_{\Sigma}(\lambda_i)}{\text{card}(M)}$$

where $\text{card}(M)$ is the number of pixels in M . If the relationship between intensity and concentration is linear, then the mean total intensity is expected to be proportional to the global concentration for long extrudates.

To transform the intensity maps into one-dimensional profiles, the distance transform of the mask is computed as already proposed by Trichard *et al.*²⁷ Let M be the set of pixel belonging to the mask and M^C be its complement. The distance transform of M , M^{DT} , is an image defined by:

32

$$M^{\text{DT}} = \left\{ y(\mathbf{x}) = \min_{\mathbf{a} \in M^C} \|\mathbf{x} - \mathbf{a}\|, \mathbf{x} \in M \right\}$$

Each pixel in the image M^{DT} contains the distance in pixels to the border of the mask M . Once the distance transform is obtained, the distance-averaged spectrum $\hat{S}(\lambda, j)$ at a distance j from the border of the pellet is computed from the full spectral map S by:

$$\hat{S}(\lambda, j) = \sum_{\mathbf{x} \in M} S(\lambda, \mathbf{x}) \delta_{j, M^{\text{DT}}(\mathbf{x})}$$

where δ is the Kronecker delta function. The distance-averaged intensity $\hat{I}(\lambda_i, j)$ may be extracted from $\hat{S}(\lambda_i, j)$ by removing the associated background. When an element is already present in the fresh support (for the case of sulfur, see section 4.4) and is fairly regularly distributed (no large spatial variation in concentration at the micron scale), the distance-averaged intensity originating from only the adsorbed species is obtained by subtracting the distance-average intensity of the fresh support.

Distance-averaged one-dimensional profiles are easier to interpret than two-dimensional maps. First, they average out the intensity fluctuations arising from the heterogeneities of the support (inclusions, cracks). Second, they are needed for comparison with one-dimensional models of diffusion.

Let J be the maximum distance to the border of the pellet:

$$J = \max_{x \in M} \{M^{\text{DT}}(x)\}$$

The distance-averaged profiles may then be plotted as a function of the distance k to the center of the pellet:

$$\hat{I}(\lambda_i, k) = \hat{I}(\lambda_i, J - j)$$

3 Results

3.1 Asphaltene impregnation

The concentration of asphaltenes in the support versus total residence time is plotted in Figure 2. Even at high temperature, the penetration of asphaltenes is very slow. The equilibrium state seems to be attained after approximately 500 h (3 weeks).

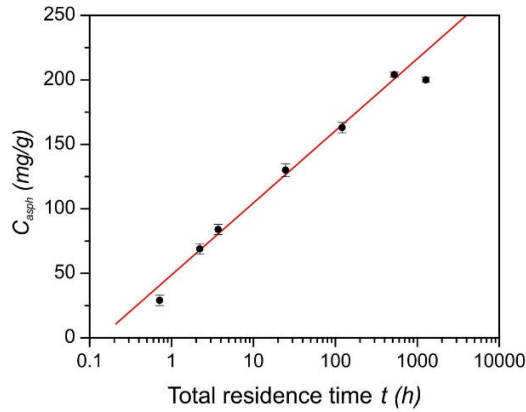


Figure 2. Asphaltene concentration in the supports versus total residence time.

Table 3 reports the quantity of impregnated asphaltenes and the global elemental concentration in the pellet as a function of time. The mass of the asphaltenes deposited on the supports was obtained by mass balance with the supernatant. The global concentrations of C, S, Ni and V on the supports were obtained by multiplying the asphaltene concentration on the support by the ele-

mental composition of the asphaltenes (Table 1). This assumes that there is no segregation of a particular element outside the catalyst extrudates during impregnation.

Table 3: Characteristics of asphaltene-impregnated supports

| Sample | 0 min | 90 min | 3 h | 1 day | 5 days | 3 weeks | 6 weeks |
|---|------------|-------------|-------------|--------------|--------------|--------------|--------------|
| Duration | 0 min | 90 min | 3 h | 24 h | 5 days | 22 days | 53 days |
| Temperature (K) | 511 | 523 | 523 | 523 | 523 | 523 | 523 |
| Pressure (MPa) | 17 | 41 | 50 | 39 | 39 | 40 | 65 |
| Mass of asphaltenes in the supports (mg) | 60 ± 2 | 121 ± 2 | 136 ± 2 | 243 ± 2 | 313 ± 2 | 396 ± 2 | 378 ± 2 |
| Asphaltene concentration in the supports (mg/g) | 29 ± 4 | 69 ± 4 | 84 ± 4 | 130 ± 5 | 163 ± 4 | 204 ± 2 | 200 ± 2 |
| Global C concentration (wt%) | 2.4 ± 0.3 | 5.7 ± 0.3 | 6.9 ± 0.3 | 10.7 ± 0.4 | 13.4 ± 0.3 | 16.8 ± 0.2 | 16.5 ± 0.2 |
| Global S concentration (ppm) | 2320 ± 660 | 5520 ± 1420 | 6720 ± 1710 | 10400 ± 2630 | 13040 ± 3280 | 16320 ± 4080 | 16000 ± 4000 |
| Global Ni concentration (ppm) | 5.5 ± 1.2 | 13.1 ± 2.2 | 16.0 ± 2.6 | 24.7 ± 4.0 | 31.0 ± 4.9 | 38.8 ± 6.1 | 38.0 ± 6.0 |
| Global V concentration (ppm) | 16.0 ± 2.6 | 38.0 ± 4.1 | 46.2 ± 4.7 | 71.5 ± 7.1 | 89.7 ± 8.4 | 112 ± 10 | 110 ± 10 |

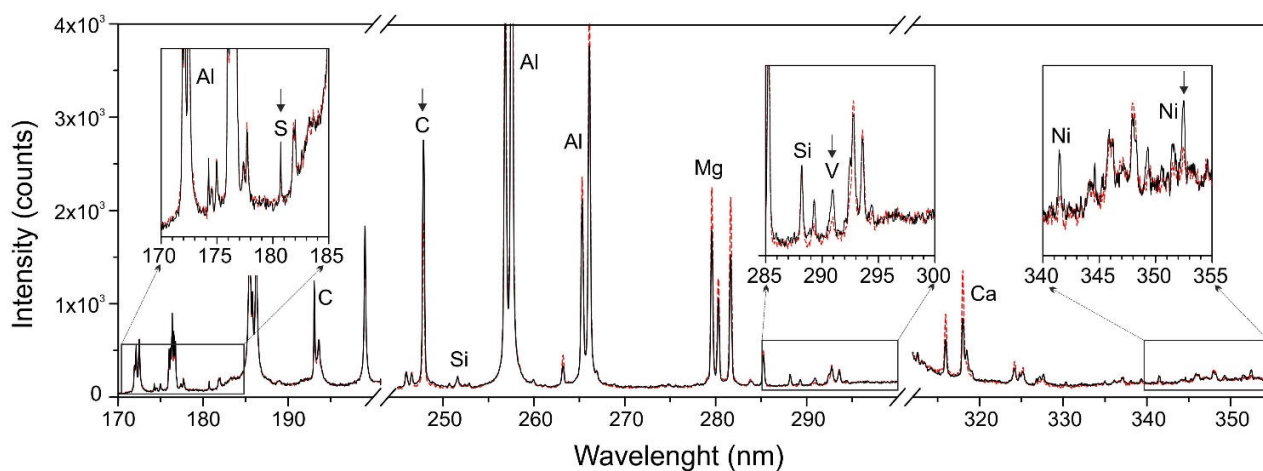


Figure 3. Typical single-shot spectra for the 3 spectral ranges investigated showing the elements of interest (S, Ni, C and V). These spectra were obtained from a pixel close to the pellet surface (black) and a pixel in the core of the pellet (red) from the 90 min sample. Each of the lines used for building the elemental map is indicated by an arrow.

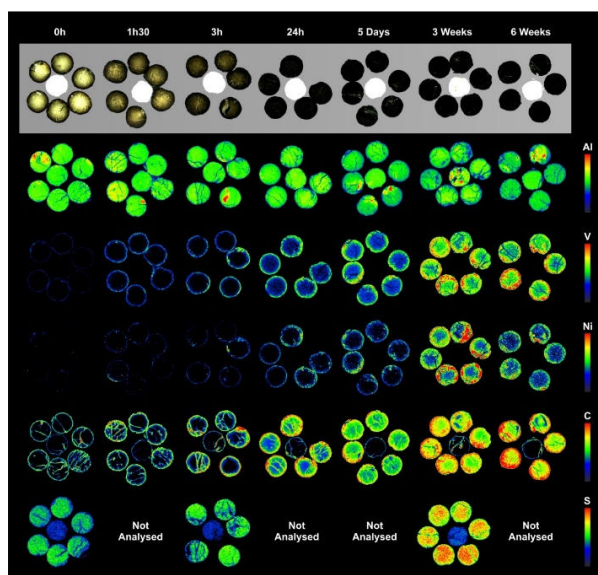


Figure 4. Optical images of supports impregnated with asphaltenes and the corresponding LIBS images of the asphaltenes. For each sample, the central extrudate is the fresh support (not impregnated)

3.2 Elemental imaging

Figure 3 shows typical spectra obtained from the 90 min sample for both a position close to the pellet surface (black full trace) and a position at the pellet core (red dotted trace). Both spectra were obtained in a single-shot configuration. Clearly, the spectral structure of these emission spectra is rather complex and presents a large dynamic range. Several lines of aluminum associated with the catalyst support, as well as lines associated with the elements of interest (C, S, Ni and V), are detected.

Optical images of the impregnated supports are shown in the top of Figure 4. The corresponding elemental images for Al, V, Ni, C and S are shown in the bottom of Figure 4. There is clearly a concentration gradient for Ni, V, and C at short impregnation times. It is obvious that such a gradient is not present for sulfur.

3.3 Calibration

The quantification strategy uses the global concentration of asphaltenes in the alumina support as a function of residence time. As mentioned before, the LIBS calibration for these samples is not straightforward because there is no homogeneous reference for such samples and because

spatially measuring such low sensitivity signals is difficult. Accordingly, we have computed the total intensities $I_{\Sigma}(\lambda_i)$ on the mask from the full spectrum maps.

Figure 5 shows the relationship between the mean total intensity $\bar{I}_{\Sigma}(\lambda_i)$ and the expected global concentration provided in Table 3.

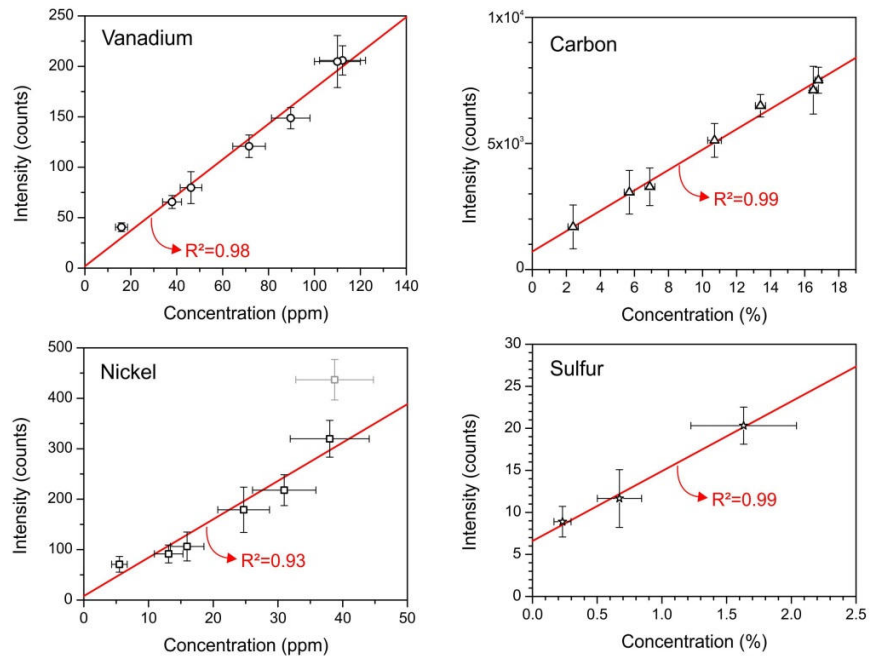


Figure 5. Calibration of LIBS intensities for V, C, Ni and S

3.4 Distance-averaged profiles

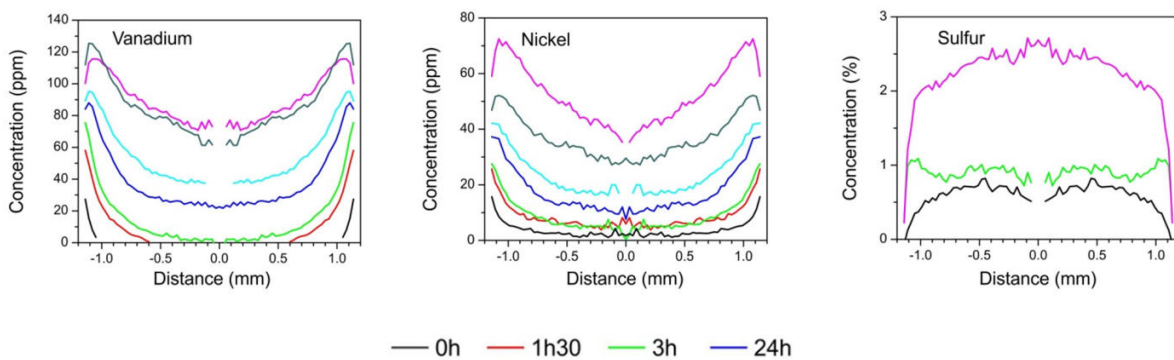


Figure 6. Distance-averaged intensity $\hat{I}(\lambda_i)$ for V, Ni and S as a function of distance from the center of the pellet for different residence times.

To average out the support heterogeneities (cracks, non-circularity of extrudates) and make a comparison with one-dimensional transport models, we extracted the intensities from distance-averaged spectra. Because of the presence of cracks and possible resin contamination, this procedure was not performed on the carbon maps. Figure 6 shows the distance-averaged profiles of V, Ni and S as a function of the distance from the center of the support for different impregnation times.

4 Discussion

4.1 Equilibration kinetics

Figure 2 clearly shows that the long impregnation time is not compatible with obtaining a catalyst with sufficient turn-over frequencies for an industrial process. Therefore, to enhance the transport properties of asphaltenes at the grain scale, industrial HDM catalysts are not only mesoporous but also macroporous.⁴ As seen in Table 3, the global concentrations of Ni and V are in the ppm range and thus require a very sensitive technique to image the concentration fields. Such concentrations are far below those reported on HDM catalysts aged 1000 h, which were on the order a few wt%.⁶⁻⁸

4.2 Elemental imaging

The single-shot spectra in Figure 3 show that the technique is sensitive enough to unambiguously detect S, Ni and V. Other impurities such as Mg, Si, and Ca are also detected. These impurities probably originate from the alumina support. Additionally, as expected for a short impregnation time, the intensities of the V and Ni lines are stronger near the pellet surface than at the core.

The optical microscopy images on the top of Figure 4 clearly reveal the changed in coloration over time, especially compared to the fresh support (central pellet). Even the first sampling with only the temperature increase and decrease (0 min) shows a slight coloration. The coloration field seems to become more homogeneous with time. For long impregnation times, the difference in coloration between samples is barely noticeable. The optical contrast response is highly nonlinear with the asphaltene concentration, which prevents us from extracting concentration fields from optical images. Importantly, the chemical heterogeneities of asphaltenes increases the complexity of the relationship between the local asphaltene concentration and the vanadium or nickel concentration.

The intensity fluctuations observed in the Al maps are interpreted as support heterogeneities such as high porosity inclusions and cracks. The S signal observed on the fresh support comes from residual sulfate species present in the support. The C images were obtained using a mask defined based on the Al map. The cracks observed in the C images are probably residue from the acrylic resin, as they can also be observed in the image of the fresh support (central pellet), which was not in contact with carbon (no asphaltene impregnation). However, the increase in the C concentration between the cracks with time can clearly be attributed to asphaltene impregnation. This difference can also be observed for each impregnation time by considering the differences between the central pellet (fresh support) and the surrounding pellets (impregnation times between 1 h 30 and 6 weeks). The cracks present in the support and the non-ideal circularity of the extrudates corroborate that the mean profile approach can average out all the geometrical support defects.

4.3 Calibration

The calibration curves of Figure 5 clearly show a linear relation between the total intensities and expected concentrations of S, Ni and V with a determination coefficient greater than 0.98 for V, C and S and equal to 0.93 for Ni. The 6 week sample was not taken into account for the Ni calibration. The origin of this outlier point is not clear. It may not be due to a problem with the impregnation process, as the other element concentrations are in line with those at previous times. Because of the presence of C and S in the native support, the calibration curves for these elements do not pass through the origin. This linear dependence allows us to further calibrate the LIBS elemental intensity and therefore transform the intensity maps into quantitative maps.

4.4 Distance-averaged profiles

The distance-averaged profiles provides a more comprehensive insight into the concentration gradients in the pellet than the elemental maps. This procedure also enhances the analysis sensitivity by averaging several spectra. Figure 6 clearly demonstrates that the equilibrium state at long residence times does not show a homogenous profile. The quantities of adsorbed Ni and V are larger close to the pellet surface than in its center. The Ni profiles are as hollow than the V profiles. On the used HDM catalysts, the deposition profiles of Ni are more homogeneous than the V profiles.⁶ These observations imply that the difference between Ni and V deposition is mainly due to differences in their reactivity within the grain instead of differences in their

transport properties. If the reactivities of the Ni and V precursors were similar, the deposition profiles of the two metals would have also been similar. For sulfur, the contribution from asphaltene is obtained by subtracting the S profiles of the impregnated supports from that of the fresh support (the non-impregnated support). The sulfur profiles are much flatter than the metals profiles, indicating that sulfur species are transported in the support much more quickly than Ni or V species.

4.5 Asphaltene transport mechanism

The interpretation of the profiles on Figure 6 using simple models of diffusion and adsorption is quite difficult. Simple diffusion models imply a flat profile at equilibrium.³³ Moreover, simple diffusion-adsorption models assume a constant concentration at the pellet surface. As the asphaltene transport is very slow and the lateral resolution of LIBS is limited (30 μm), the apparent concentration at the very first point near the surface is an average of the first 30 μm , and a very steep gradient therefore may be blurred. However, at long impregnation times, these steep gradients should disappear. This is not what is observed. These observations suggest that there are mechanisms other than simple reversible adsorption and diffusion.

One hypothesis to explain the continuously increasing concentrations at the pellet surface is the aggregation of the asphaltene. Asphaltene may aggregate in solution even at high temperature, and their disaggregation kinetics are much slower than the rate of transporting an isolated asphaltene molecule to the center of the pellet. The liquid phase then provides a large reservoir of isolated asphaltene, but they are produced with extremely slow kinetics. Another hypothesis may be the irreversibility of the adsorption of the asphaltene on the supports. Irreversible adsorption will lead to a concentration gradient with higher concentrations close to the pellet surface. A kind of “stop and go” mechanism is suspected.³⁴ The final hypothesis involves the heterogeneity of asphaltene. Simple models imply a single species with a well-defined diffusion coefficient and well-defined adsorption on the surface. Small asphaltene with low metal concentrations are transported quickly, whereas large ones rich in metals are transported much slower; this behavior may lead to the hollow profiles observed at long impregnation times. Thus, to explain the experimental Ni and V profiles, a complex transport model that considers irreversible adsorption and/or asphaltene disaggregation kinetics and/or asphaltene heterogeneities is required. Owing to

the distance-averaged profiles, such models can be one-dimensional, which will simplify their development.

Modeling internal diffusion-limited processes requires having a model at the grain scale that considers the transport of species and their reactions. It is impossible to decouple these two phenomena if the model parameters are adjusted according to catalytic tests. The extreme sensitivity of LIBS allows us to explore the first steps of the catalytic process: diffusion and adsorption on the active sites. The methodology proposed in this work for the supports of HDM catalysts may be applied to other fields. The extension of LIBS mapping to other catalytic systems is also possible since any element can be excited by the plasma and produce emission lines. Only the sensitivity is dependent on the element. In addition, elements such as hydrogen, oxygen and carbon require special care, as they are present in the embedding resin. Particular sample preparation methods need to be employed to overcome these limitations, especially for studies involving hydrocarbons. In general, such results could not be obtained with more conventional imaging approaches such as electron probe microanalysis EPMA because of both the sensitivity required for Ni and V (limit of detection ~10 ppm) and the very low sensitivity for light elements such as C. In addition, technological developments in LIBS are expected, such as the use of higher repetition rate lasers (100 Hz) and faster and more sensitive detectors. Because of their speed, compactness, atmospheric operability and reasonable acquisition and operating costs, LIBS mapping systems are expected to play an essential role in the spatially resolved analysis of catalysts in the forthcoming years.

5 Conclusion

Using a self-pressurized autoclave, we impregnated a mesoporous alumina support with asphaltenes at high pressure and high temperature. The transport of asphaltenes in the support was very slow. Using LIBS allowed the imaging of the distribution of S, Ni, V, C and Al in the pellet. The sensitivity of LIBS was found to be adequate to detect Ni and V, which are present on these supports in the ppm range. Using the distance transform of the mask of the pellets, we transformed the two-dimensional maps into one-dimensional profiles, thereby simplifying the discussion of the transport dynamics and allowing the comparison with simple transport models. The sulfur precursors were found to be transported much quicker than the metal precursors, leading to flat instead of hollow profiles. The Ni profiles are found to be as hollow as the vanadium ones, which

suggests that the difference observed on the used HDM catalyst originates from the lower reactivity of the Ni precursors rather than faster transport. The experimental profiles could not be explained by a simple model that considers diffusion and reversible adsorption. Other phenomena such as irreversible adsorption and/or slow disaggregation kinetics and/or asphaltene heterogeneities may also occur in this system.

We believe that the potential of LIBS for imaging the precursor distribution in a catalyst has the potential to help decouple transport and reactivity in heterogeneous catalysis. It should enhance the design of reactivity models at the grain scale with more robust parameter identification.

Supplementary information

The spectrometer parameters and optical emission lines used in this study are available as supplementary information.

Corresponding Author

* loic.sorbier@ifpen.fr

Author Contributions

The manuscript was written through contributions of all authors.

Abbreviations

HDM, hydrodemetallization; LIBS, laser-induced breakdown spectroscopy

References

- (1) Dingerdissen, U.; Martin, A.; Herein, D.; Wernicke, H. The Development of Industrial Heterogeneous Catalysis. In *Handbook of Heterogeneous Catalysis*, 2nd ed.; Ertl, G., Knozinger, H., Schuth, F., Weitkamp, J. Eds.; Wiley-VCH: Weinheim, 2008; pp 37–38.
- (2) Weckhuysen, B., *Angew. Chem., Int. Ed.* **2009**, 48, 4910–4943
- (3) Leyva, C.; Rana, M.; Trejo, F.; Ancheyta, J.; *Catal. Today* **2009**, 141, 168–175.
- (4) Merdrignac, I.; Roy-Auberger, M.; Guillaume, D.; Verstraete, J.; Hydroprocessing and Hydroconversion of Residue Fractions. In *Catalysis by Transition Metal Sulphides*; Toulhoat, H., Raybaud, P. Eds.; Editions Technip: Paris, 2013; pp 679–737.

- (5) Mullins, O. C.; Sabbah, H.; Eyssautier, J.; Pomerantz, A. E.; Barre, L.; Andrews, A. B.; Ruiz-Morales, Y.; Mostowfi, F.; McFarlane, R.; Goual, L.; Lepkowicz, R.; Cooper, T.; Orbulescu, J.; Leblanc, R. M.; Edwards, J.; Zare, R. N. *Energy Fuels* **2012**, 26, 3986–4003.
- (6) Furimsky, E.; Massoth, F. *Catal. Today* **1999**, 52, 381–495.
- (7) Tamm, P.; Harnsberger, H.; Bridge, A. *Ind. Eng. Chem. Process Des. Dev.* **1981**, 20, 262–273.
- (8) Sorbier, L.; Bazer-Bachi, F.; Moreaud, M.; Moizan-Basle, V. *Chem. Eng. Sci.* **2016**, 155, 186–193.
- (9) Baltus, R. E.; Anderson, J. L. *Chem. Eng. Sci.* **1983**, 38, 1959–1969.
- (10) Marchal, C.; Abdessalem, E.; Tayakout-Fayolle, M.; Uzio, D. *Energy Fuels* **2010**, 24, 4290–4300.
- (11) Roussi, L.; Stihle, J.; Geantet, C.; Uzio, D.; Tayakout-Fayolle, M. *Fuel* **2013**, 109, 167–177.
- (12) Tayakout, M.; Ferreira, C.; Espinat, D.; Picon, S. A.; Sorbier, L.; Guillaume, D.; Guibard, I. *Chem. Eng. Sci.* **2010**, 65, 1571–1583.
- (13) Gaulier, F.; Barbier, J.; Guichard, B.; Levitz, P.; Espinat, D. *Energy Fuels* **2015**, 29, 6520–6528.
- (14) Goldstein, D.; Newbury, D.; Joy, D.; Lyman, C.; Echlin, P.; Lifshin, E.; Sawyer, L.; Michael, J.; *Scanning Electron Microscopy and X-ray Microanalysis*, 3rd ed. ; Springer: New York 2003.
- (15) Janssens, K.; De Nolf, W.; Van Der Snickt, G.; Vincze, L.; Vekemans, B.; Terzano, R.; Brenker, F. *Trends Anal. Chem.* **2010**, 29, 464–478.
- (16) Sancey, L.; Motto-Ros, V.; Busser, B.; Kotb, S.; Benoit, J. M.; Piednoir, A.; Lux, F.; Tillement, O.; Panczer, G.; Yu, J. *Sci. Rep.* **2014**, 4, 6065.
- (17) Sancey, L.; Kotb, S.; Truillet, C.; Appaix, F.; Marais, A.; Thomas, E.; van der Sanden, B.; Klein, J.P.; Laurent, B.; Cottier, M.; Antoine, R.; Dugourd, P.; Panczer, G.; Lux, F.; Perriat, P.; Motto-Ros, V. Tillement, O. *ACS Nano* **2015**, 9, 2477–2488.
- (18) Ma, Q.L.; Motto-Ros, V.; Lei, W.Q.; Boueri, M.; Zheng, L.J.; Zeng, H.P.; Bar-Matthews, M.; Ayalon, A.; Panczer, G.; Yu, J. *Spectrochim. Acta, Part B* **2010**, 65, 707–714.
- (19) Bassel, L.; Motto-Ros, V.; Trichard, F.; Pelascini, F.; Ammari, F.; Chapoulie, R.; Ferrier, C.; Lacanette, D.; B. Bousquet, B. *Environ. Sci. Pollut. Res.* **2016**, doi:10.1007/s11356-016-7468-5.
- (20) Lucena, P.; Vadillo, J.M.; Laserna, J.J. *Anal. Chem.* **1999**, 71, 4385–4391.
- (21) Lucena, P.; Laserna, J.J.; *Spectrochim. Acta, Part B* **2001**, 56, 177–185.
- (22) Lucena, P.; Vadillo, J.M.; Laserna, J.J. *Appl. Spectrosc.* **2001**, 55, 267–272.

- (23) Lucena, P.; Vadiillo, J.M.; Laserna, J.J. *J. Anal. At. Spectrom.* **2002**, 17, 548–551.
- (24) Noll, R.; Bette, H.; Brysch, A.; Kraushaar, M.; Mönch, I.; Peter, L.; Sturm, V. *Spectrochim. Acta, Part B* **2001**, 56, 637–649.
- (25) Menut, D.; Fichet, P.; Lacour, J.L.; Rivoallan, A.; Mauchien, P. *Appl. Opt.* **2003**, 42, 6063–6071.
- (26) Kim, T.; Lin, C.T.; Yoon, Y. *J. Phys. Chem. B* **1998**, 102, 4284–4287.
- (27) Trichard, F.; Sorbier, L.; Moncayo, S.; Blouët, Y.; Lienemann, C.P.; Motto-Ros, V. *Spectrochim. Acta, Part B* **2017**, 133, 45–51
- (28) Brunauer, S.; Emmett, P. H.; Teller, E. *J. Am. Chem. Soc.* **1938**, 60, 309–319.
- (29) Barrett, E. P.; Joyner, L. G.; Halenda, P. P. *J. Am. Chem. Soc.* **1951**, 73, 373–380.
- (30) Motto-Ros, V.; Negre, E.; Pelascini, F.; Panczer, G. ; Yu, J. *Spectrochim. Acta, Part B* **2014**, 92, 60–69.
- (31) Trichard, F.; Moncayo, S.; Devismes, D.; Pelascini, F.; Maurelli, J.; Feugier, A.; Sasseville, C.; Surma, F.; Motto-Ros V. accepted in *JAAS* **2017**, <https://doi.org/10.1039/C7JA00185A>
- (32) Rosenfeld, A.; Pfaltz, J. *J. Assoc. Comput. Mach.* **1966**, 13, 471–494.
- (33) Crank, J. *The Mathematics of Diffusion*; Clarendon Press, Oxford, 1975.
- (34) Barbier, J.; Gaulier, F.; Guichard, B.; Levitz, P.; Espinat, D. *Energy Fuels* **2017**, 31, 7426–7437.